Seismic Efficiency and Seismic Moment for Small Craters on Mars Formed in the Layered Uppermost Crust

A. Rajšić, K. Miljković, N. Wójcicka, G. Collins, Raphael F Garcia, C. Bredemeyer, A. Lagain, I. Daubar, Philippe Lognonné

JGR Planets

RESEARCH ARTICLE
10.1029/2022JE007698

Seismic Efficiency and Seismic Moment for Small Craters on Mars Formed in the Layered Uppermost Crust

A. Rajšić[1,2], K. Miljković[2], N. Wójcicka[3], G. S. Collins[3], R. F. Garcia[4], C. Bredemeyer[2], A. Lagain[2], I. J. Daubar[5], and P. Lognonné[6]

[1]Department of Earth, Atmospheric and Planetary Sciences, Purdue University, West Lafayette, IN, USA, [2]School of Earth and Planetary Sciences, Space Science and Technology Center, Curtin University, Perth, WA, Australia, [3]Imperial College London, London, UK, [4]Institut Supérieur de l'Aéronautique et de l'Espace (ISAE-SUPAERO), Université de Toulouse, Toulouse, France, [5]Department of Earth, Environmental and Planetary Sciences, Brown University, Providence, RI, USA, [6]Institute de Physique du Globe de Paris, Paris, France

Abstract Seismic activity generated by impacts depends on impact conditions and properties of the impact site. Here, we combined mapping of the regolith thickness with numerical impact simulations to better estimate the seismic efficiency and seismic moment generated in small impact events in the uppermost crust on Mars. We used mapping of crater morphology to determine the regolith thickness that craters formed in. We found that local regolith thickness in the late Amazonian units is between 4 and 9 m. Combined with previous estimates for the NASA InSight landing site, we composed a more realistic uppermost crust analog and implemented it in numerical impact simulations. We estimated the seismic efficiency and seismic moment for small craters on Mars impacting a non-porous or fractured bedrock overlaid by 5, 10, or 15 m thick regolith. Seismic energy showed more dependence on target properties. Three orders of magnitude more energy were produced in stronger targets. The seismic moment does not depend on target properties, and we confirm that seismic moment is almost proportional to impact momentum. The resulting seismic moment is in agreement up to a factor of 4 between different target types. We improved the scaling relationships developed from numerical simulations used in seismic moment approximations by constraining its dependence on more realistic target properties.

Plain Language Summary Small impacts form in the top few meters of the crust of Mars. From the NASA InSight mission data, we learned that the uppermost crust of Mars is layered. Here, we mapped and used rocky ejecta craters as a proxy to estimate the thickness of this top layer. We demonstrated that a younger, late Amazonian geological unit, has a thinner top regolith layer (4–9 m) compared to an older, Hesperian unit (3–17 m). We modeled several target scenarios, constrained by mapping results, and performed a suite of numerical simulations of small impacts. From these simulations, we determined a relationship between impact-generated seismic energy and the seismic moment for different types of Martian upper-crust analogs. Our models show that impact-generated seismic energy strongly depends on target properties (three orders of difference among different analogs investigated here). On the contrary, seismic moment shows agreement up to a factor of 4 in different targets. We discussed our modeling results to the newly detected impacts on Mars, and confirmed that our models are reliable for predicting seismic moments of small impacts. Our results contribute to the understanding of the size and energy of impact-generated seismic sources in different target analogs.

Key Points:

- Using rocky ejecta craters, we mapped regolith thickness on Mars and found that in the late Amazonian volcanic unit, it is 4–9 m
- Seismic efficiency shows larger sensitivity on target properties (up to three orders of magnitude) than the seismic moment (factor of four)
- A comparison of numerical simulations with the new seismic detections of craters on Mars showed agreement with our models

Supporting Information:

Supporting Information may be found in the online version of this article.

Correspondence to:

A. Rajšić,
arajsic@purdue.edu

Citation:

Rajšić, A., Miljković, K., Wójcicka, N., Collins, G. S., Garcia, R. F., Bredemeyer, C., et al. (2023). Seismic efficiency and seismic moment for small craters on Mars formed in the layered uppermost crust. *Journal of Geophysical Research: Planets*, *128*, e2022JE007698. https://doi.org/10.1029/2022JE007698

Received 30 NOV 2022
Accepted 17 MAR 2023

Author Contributions:

Conceptualization: A. Rajšić
Data curation: A. Rajšić, R. F. Garcia
Formal analysis: A. Rajšić
Funding acquisition: K. Miljković
Investigation: A. Rajšić
Methodology: A. Rajšić, N. Wójcicka, G. S. Collins
Supervision: K. Miljković, G. S. Collins
Validation: A. Rajšić, R. F. Garcia
Visualization: A. Rajšić
Writing – original draft: A. Rajšić

1. Introduction

Impact cratering is a complex process during which the impactor's momentum and kinetic energy are delivered to the target (e.g., Melosh, 1989). Understanding the transfer of the impact's kinetic energy to the target on a planetary body helps estimate the seismic properties of the planet's crust. Several hundreds of impacts were previously detected in Apollo seismic data (e.g., Duennebier & Sutton, 1974; Latham et al., 1970). The investigation of the Apollo seismic data showed that the understanding of impact-induced seismic source-time function (e.g., Gudkova et al., 2015), seismic moment (e.g., Teanby, 2015, and references there in), and the seismic efficiency in a target medium (e.g., Latham et al., 1970) are a prerequisite to describe impacts in seismic data.

Interest in natural impacts on planetary surfaces and their seismic signatures has increased with the placement of NASA InSight's seismometer on Mars in late 2018 (e.g., Banerdt et al., 2020). It was expected that one of the possible sources of seismic activity would be impacts (e.g., I. Daubar et al., 2018, and references therein). Since

Writing – review & editing: A. Rajšić, K. Miljković, N. Wójcicka, G. S. Collins, R. F. Garcia, C. Bredemeyer, A. Lagain, I. J. Daubar, P. Lognonné

the NASA InSight landing on Mars (Banerdt et al., 2020), several hundreds of seismic events were recorded (Clinton & Euchner, 2021). During the first year of InSight operating on Mars, none of these events were related to impacts (I. Daubar et al., 2020). Recently, several impacts were confirmed in seismic data (Garcia et al., 2022; Posiolova et al., 2022). Detectability of small impacts on Mars in seismic data can be better constrained with further investigations of: (a) the impact-generated pressure wave decay, (b) the seismic efficiency in target media, (c) the relationship between seismic moment and impact momentum, and (d) the relationship between seismic moment and seismic energy.

The seismic efficiency, k, is quantified as the fraction of the impact energy turned into seismic energy (e.g., McGarr et al., 1969; P. Schultz & Gault, 1975). Estimates of seismic efficiency of impacts from a variety of studies range widely, from 10^{-6} to 10^{-1} (I. Daubar et al., 2018; Güldemeister & Wünnemann, 2017; Hoerth et al., 2014; Matsue et al., 2020; McGarr et al., 1969; Pomeroy, 1963; Richardson & Kedar, 2013; P. Schultz & Gault, 1975; Shishkin, 2007; Yasui et al., 2015). In previous work (Rajšić, Miljković, Collins, et al., 2021; Rajšić, Miljković, Wójcicka, et al., 2021), appropriate for analogs of the uppermost crust on Mars and the Moon, we showed that the seismic efficiency varies three orders of magnitude between non-porous, bedrock-like targets ($\sim 10^{-3}$), and highly porous targets that represent regolith ($\sim 10^{-6}$), assuming a homogeneous target.

In this work, we consider strictly vertical impacts and focus on calculating the vertical component of the seismic moment as proposed by previous works (Gudkova et al., 2011, 2015; Lognonné et al., 2009). Comparing data from impact simulations and previously published data (e.g., Teanby & Wookey, 2011, and refs therein), Wojcicka et al. (2020) presented the relationship between seismic moment M (Nm) and impact momentum p_i (kg m s^{-1}), for impacts into regolith-like targets:

$$M = 10^{3.1\pm0.08} p_i^{1.0\pm0.01} \tag{1}$$

Teanby and Wookey (2011) derived a relationship that relates seismic moment (M) and seismic energy (E_s) using published data on small earthquakes, numerical simulations, and nuclear explosions (Abercrombie, 1995; Mayeda & Walter, 1996; Patton & Walter, 1993; Walker, 2003):

$$E_s = 4.8^{+2.9}_{-1.8} \times 10^{-9} M^{1.24\pm0.01} \tag{2}$$

For regolith-like targets, Wojcicka et al. (2020) proposed the following relationship, that was derived for small impacts in single porous (44% porosity) target analogs:

$$E_s = 10^{-7.6} M^{1.2} \tag{3}$$

Numerical simulations were also compared to artificial impacts on the Moon (Rajšić, Miljković, Wójcicka, et al., 2021). The seismic efficiency was calculated for lunar regolith-like targets to be on the order of 10^{-6}, which is consistent with lower estimates of Latham et al. (1970). Similarly, the seismic moment was estimated to be at the order of 4×10^{10} Nm, which was in agreement with Equations 2 and 3 (Teanby, 2015; Wojcicka et al., 2020) for regolith-like targets.

For a variety of other geological units, ages, and types, the regolith thickness may be diverse. Crater mapping and geological observations showed that a layer of regolith covers Martian surface, and that in the vicinity of the InSight lander, the top regolith layer ranging between 3 and 17 m in thickness covering stronger substrates (Golombek et al., 2020; Warner et al., 2017). This was a regional/local estimate (early Hesperian unit (Tanaka, Skinner, Dohm, et al., 2014)). There seems to be a discontinuity in the target strength between layers that can affect the cratering process and final crater morphology. In comparison to the homogeneous analogs investigated before, layered targets may exhibit different seismic properties.

In this work:

- We estimated the regolith thickness in a younger, late Amazonian volcanic unit, to complement the regolith thickness estimation for the older Hesperian unit, where InSight landed; We combined our regolith thickness estimates with those of Warner et al. (2017), and applied layered target analogs in our numerical models;
- We made a series of numerical impact simulations of small craters on Mars formed in layered targets;
- We quantified seismic energy and seismic moment produced by small impacts in layered upper crust analogs on Mars;

- We defined a relationship between impact momentum and seismic moment, and between seismic moment and seismic energy, in a range of layered Martian upper crust analogs, expanding on previous works;
- Finally, we show that newly detected impacts in seismic data on Mars fit within our numerical modeling estimates of the seismic moment.

2. Regolith Thickness Mapping

Estimates of the regolith thickness have been done in the past using morphological observations (e.g., Bart et al., 2011; Quaide & Oberbeck, 1968; Yasui et al., 2015), crater mapping (e.g., Shoemaker et al., 1969), and lunar seismic data (e.g., Cooper et al., 1974; Watkins & Kovach, 1973). Here we investigated rocky ejecta craters (RECs), characteristic of bedrock excavation during cratering (e.g., Rennilson et al., 1966; Shoemaker & Morris, 1970; Wilcox et al., 2005). Their identification on planetary surfaces suggests distinct layering with depth from regolith to bedrock and can be used to estimate the thickness of the top regolith layer. While RECs can be used to estimate regolith thickness, there is still concern about how long they have been exposed to the surface and, thus, to erosion or burial processes. In this work, the REC method to estimate the regolith thickness was combined with additional classification on the degradation of the craters as recommended in Warner et al. (2017). While Warner et al. (2017) uses five different degradation classes, where class one being the least degraded and class five being the most degraded, we focused our search of RECs only on the freshest ones, that is, classes I and II (Figures 1 and 2 in this work, and Figure 12 in Warner et al. (2017)).

We first classify craters as REC and non-rocky ejecta craters (nREC). RECs were used to estimate the maximum regolith thicknesses, and nRECs to confirm the onset diameter where a weaker layer is excavated. The lack of boulders in the ejecta of nRECs indicates that they did not excavate stronger substrate beneath the regolith, so we use them to calculate the minimum regolith thickness. In both cases, we focus our search on the freshest craters (class I and II of Warner et al. (2017)). Although secondary craters resulting from distal ejecta of large impacts might exhibit boulders and be identified as RECs, they do not form with the same impact conditions as primary craters (velocity, angle). To ensure that the boulders around RECs come from the excavation of the stronger substrate rather than from another crater in the vicinity of the mapping area, only craters where boulders were around the crater rim, on the rim, and falling back to the crater cavity were mapped (Figure 1, red arrows and circles). In addition, we mapped an area outside of major secondary crater clusters identified by Lagain et al. (2021) using a machine learning crater identification algorithm (Benedix et al., 2020). To estimate the regolith thickness, Warner et al. (2017) used an approach that suggests that ejecta is sourced from 0.084 times the measured crater diameter. Here, we bounded regolith estimates using a factor derived by Warner et al. (2017), but we also considered experimental works that suggested a lower (0.06) and higher bound (0.09) (Grieve et al., 1981; Hermalyn & Schultz, 2011; P. H. Schultz & Anderson, 1996). The same method showed that the top regolith layer is between 3 and 17 m in thickness, proximal to the InSight lander (Golombek et al., 2020; Warner et al., 2017).

We mapped RECs 700 km away from the InSight lander at 6.5°N, 148°E. For mapping, we used High-resolution imaging experiment, McEwen et al., 2007) image: `ESP_047376_1865` (Figure 3), with a pixel scale of 0.5 m/pixel. This area was selected because one new crater was confirmed in CTX images between August 2019 and September 2020 (before: `K20_061156_1866_XN_06N212W` (13 August 2019); after: `N10_066088_1840_XN_04N211W` (01 September 2020) (I. Daubar et al., 2022)). We mapped the older HiRISE image because, at the time of the CTX confirmation, it was only available, and we aimed to see how thick the regolith layer in the area was and how it would affect the detectability of the formed impact, following our work in Rajšić, Miljković, Collins, et al. (2021). This impact was not confirmed in the seismic data, so we used our regolith thickness estimates to compare to Warner et al. (2017) regolith thickness measurements and to make more realistic numerical models.

For crater mapping, we used the Environmental Systems Research Institute's (ESRI's) ArcMap (ArcGIS), version 10.6, with included the Crater Tools extension (Kneissl et al., 2011). Crater Tools were used to record crater diameters. Crater diameters were digitized using the "circle by points" method. In this method, using any three points on the crater rim, the tool approximates a circle and records the diameter of the crater. This tool is useful since it eliminates errors caused by different map projections (Kneissl et al., 2011).

We measured the diameters of 1,155 simple craters and classified them as rocky ejecta (RECs) and nRECs (list of all the mapped craters is in online repository Rajšić (2022)). RECs were used to estimate maximum regolith thickness and nRECs minimum (Warner et al., 2017). The smallest crater had a diameter of 2 m and the largest

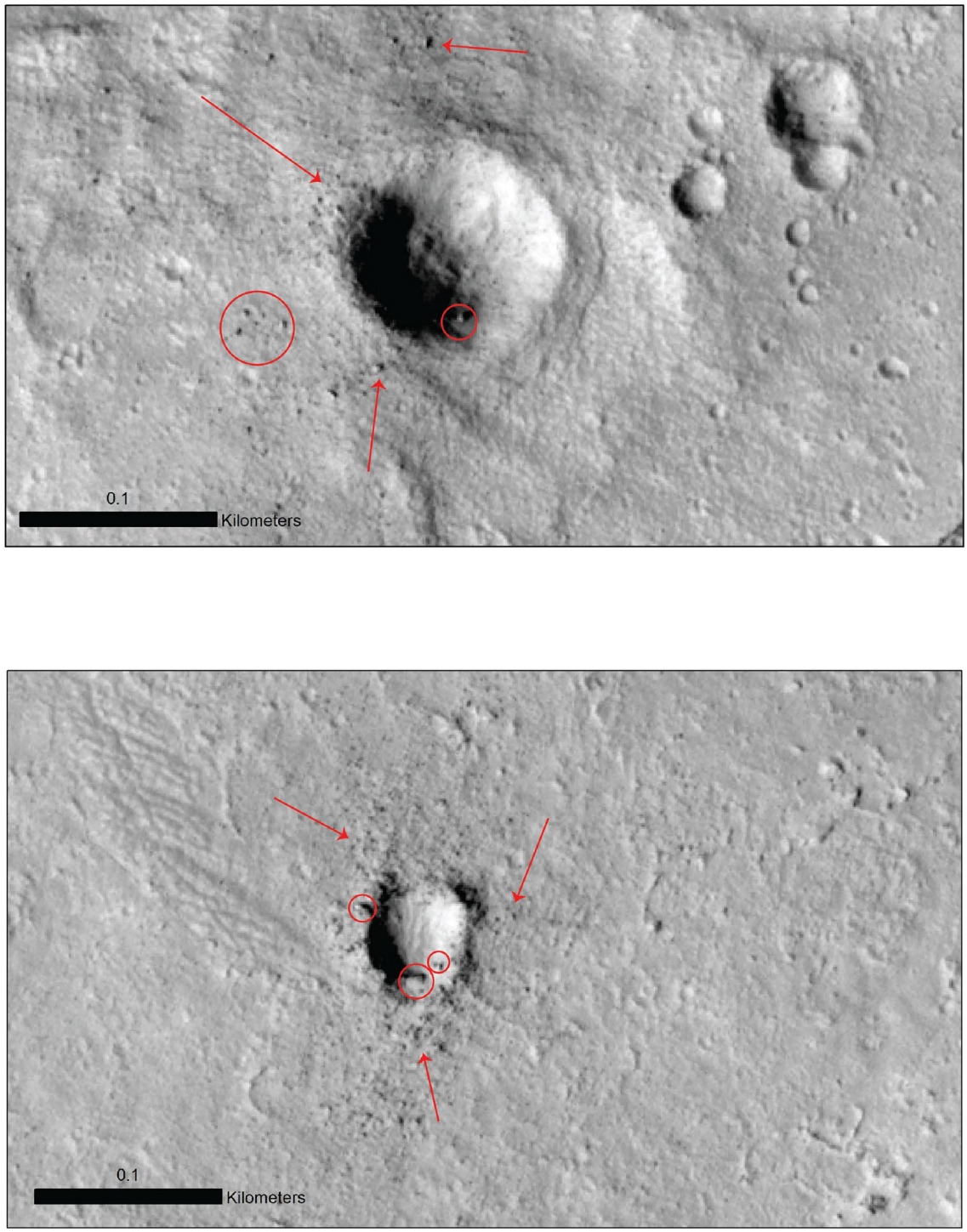

Figure 1. Characteristics of the rocky ejecta craters classified as the first class according to Warner et al. (2017) (HiRISE image ESP_047376_1865). Note these are both very fresh-looking craters. On both craters, rocks around the crater and falling back to the cavity are marked. The Crater rim is fresh, and rocks are exposed to it.

103 m. The median diameter was 10 m. Most of the measured craters are between 5 and 15 m in diameter. Of these, only 1.4% (16 craters total) were RECs (Table 1). The smallest and largest RECs were 15.3 and 103 m in diameter, respectively. The smallest and largest nREC were 2 and 48 m in diameter, respectively.

Table 1 shows the measured REC diameters used to estimate the crater excavation depth. The lower bound for the regolith thickness estimate was measured as crater diameter multiplied by a factor of 0.06 and for the upper

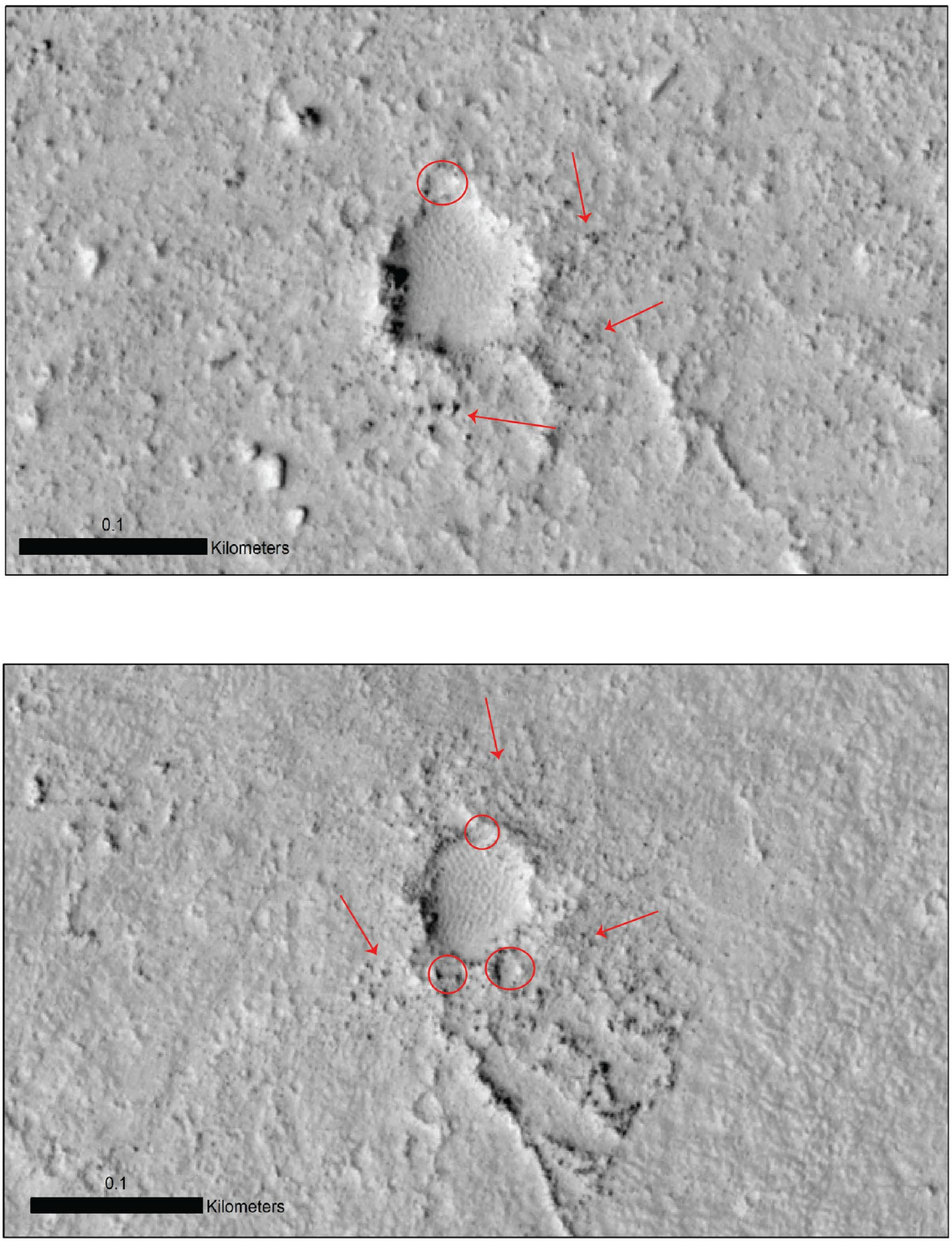

Figure 2. Characteristics of the rocky ejecta craters (RECs) classified as the second degradation class according to Warner et al. (2017) (HiRISE image ESP_047376_1865). Note these are both very fresh-looking craters. The main difference is the slow degrading of the crater rim and infilling of the cavity, which can be followed by the presence of younger craters superposed on the rim or the ejecta of the second class REC.

bound, the diameter was multiplied by a factor of 0.09 (Grieve et al., 1981; Hermalyn & Schultz, 2011; P. H. Schultz & Anderson, 1996). For the lower bound estimate, 0.06, the regolith thickness varied between 0.92 and 6.16 m. If the ejecta material was sourced from a larger depth (factor 0.09), the regolith thickness varied between 1.37 and 9.24 m. An average estimate was made with the approach of Melosh (1989), where the excavation

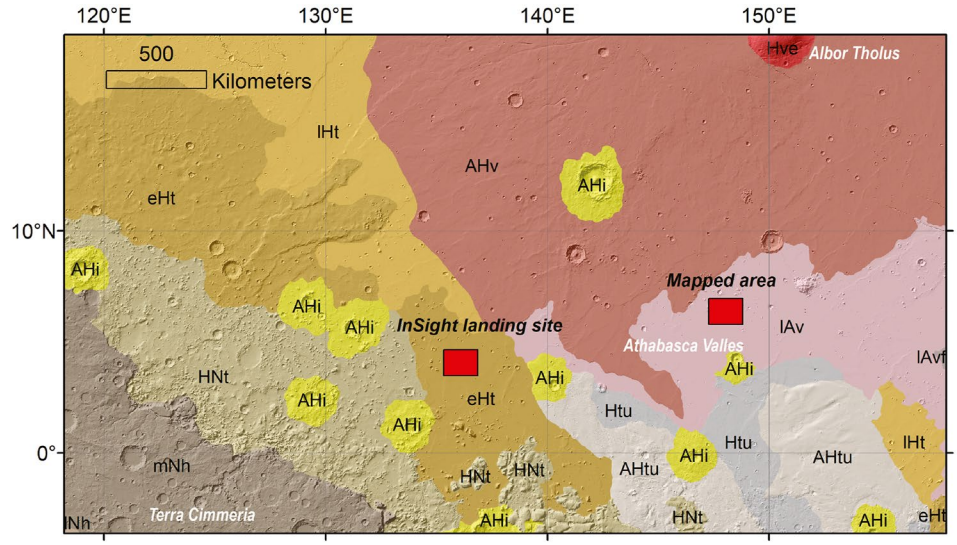

Figure 3. Geological map of a wider area surrounding the InSight landing site (early Hesperian transition Unit). Mapped area is approximately 1,000 km eastern from the lander (late Amazonian volcanic unit). (For details about notation used for geological units, see Tanaka, Skinner, et al. (2014)). Geological unit map overlays the Mars Orbiter Laser Altimeter shaded relief (Smith et al., 2001).

Table 1
Rocky Ejecta Crater (Rocky Ejecta Craters) Diameters Obtained From Crater Mapping and Estimated Regolith Thicknesses

Crater ID	REC diameter (m)	Regolith thickness (exp. lower) (m)	Regolith thickness (theory) (m)	Regolith thickness (exp. upper) (m)
471	73	4.36	6.10	6.54
488	75	4.49	6.28	6.73
582	103	6.16	8.62	9.24
679	28	1.68	2.35	2.51
768	52	3.13	4.39	4.70
775	34	2.03	2.84	3.04
893	44	2.66	3.73	4.00
894	61	3.69	5.16	5.53
895	31	1.87	2.62	2.80
896	44	2.64	3.69	3.96
897	73	4.41	6.17	6.61
898	19	1.11	1.55	1.66
899	15	0.92	1.28	1.37
900	58	3.48	4.87	5.22
990	47	2.80	3.9	4.20
901	36	2.15	3.01	3.22

Note. The minimum regolith thickness was calculated with a factor of 0.06 of transient crater diameter, average with a factor of 0.084, and maximum with a factor of 0.09 (Melosh, 1989; Warner et al., 2017). For details see: Rajšić (2022).

depth was considered to be 0.084 times the crater diameter. In this case, the regolith thickness is estimated to be between 1.28 and 8.62 m. However, to compare with previous works, the cut-off regolith thickness is considered to correspond to the maximum nREC diameter. The largest nREC crater in this area is 48 m in diameter. Thus, we adopted the lower bound of excavation depth for the whole area to be between 2.9 and 4.3 m using different factors in the regolith thickness-crater diameter relationship. Images of the mapped REC craters used in this work are part of Figures S1–S8 in Supporting Information S1.

Our mapping area is in the late Amazonian volcanic unit (e.g., Tanaka, Skinner, Dohm, et al., 2014), while InSight landing site (3–17 m regolith thickness (e.g., Warner et al., 2017)) is in early Hesperian transition unit. This result suggests that the younger geological units may have a thinner regolith layer, most likely due to shorter exposure to impact gardening, one of the main processes involved in regolith production. We combined our estimate (since these units surround InSight lander) with the estimate of Warner et al. (2017) and vary regolith thickness between 5 and 15 m in our numerical models to be applicable to a wide variety of targets in the InSight region.

3. Numerical Simulations of Small Impacts in Layered Targets

We present impact simulations focused on pressure wave propagation in layered targets. The simulations were made using the shock physics code iSALE-2D (e.g., Amsden et al., 1980; Collins et al., 2004; Wünnemann et al., 2006). The numerical impact setup was similar to our previous works made for calculating pressure propagation to several crater radii, without focusing on the crater formation itself (Rajšić, Miljković, Collins, et al., 2021; Wojcicka et al., 2020). It is considered that at this distance, pressure amplitude is comparable to the strength of the material (e.g., Holsapple, 1993; Rajšić, Miljković, Collins, et al., 2021; Yasui et al., 2015). The purpose was

Table 2
Impact Conditions Used in This Work

Simulation	Impactor radius (m)	Vertical velocity (m s^{-1})	Rim diameter (sand, m)	Rim diameter (regolith, m)
1	0.044	2,000	2.56	1.60
2	0.072	3,300	4.61	3.22
3	0.10	4,150	6.60	4.90
4	0.19	5,370	12.1	9.89
5	0.49	6,380	28.3	25.5

Note. Following Wojcicka et al. (2020), these are derived from impact crater scaling relationships and include atmospheric effects on incoming impactor size and speed.

to observe the pressure wave dissipation at a distance from the impact point. This required a large numerical mesh. The size of the computational domain varied between 3000 × 3000 cells and 4000 × 4000, depending on the projectile size. Here, we model impacts with projectiles between 4.4 and 49 cm in radius (Table 2) using the resolution of 10 cells per projectile radius to offset the computational demand for the large mesh. Numerical resolution tests for this kind of simulation were made in our previous works (Rajšić, Miljković, Collins, et al., 2021).

During the lifetime of the InSight mission, it was expected that the largest crater diameter to form would likely be smaller than 30 m in diameter (I. Daubar et al., 2013; I. Daubar et al., 2018; I. J. Daubar et al., 2014), except for the most recent two 130–150 m craters (Posiolova et al., 2022). For rocky meteoroids that could form craters up to 30 m, the atmospheric drag and ablation are expected to substantially reduce the impact speed on the ground from an average of 11 to approximately 2–5 k m s^{-1} (I. Daubar et al., 2020; Wojcicka et al., 2020). These values were defined assuming a typical meteoroid density of 2,700 kg m^{-3}, pre-entry speed of 10 k m s^{-1} and angle of 45° (McMullan & Collins, 2019). Here, we simulated five different impact scenarios, where final crater sizes were estimated from known scaling laws (see, Wojcicka et al. (2020)). Input parameters and crater sizes are shown in Table 2.

All impact scenarios were simulated in several different upper-crust Martian analogs. Here, we investigated possible impact scenarios needed to form craters up to 30 m in diameter in single-layer, bedrock, and fractured bedrock targets, as well as in layered targets appropriate for REC morphology. We applied a two-layered approach, where the upper layer of regolith varies in thickness between 5, 10, and 15 m. All impact conditions were tested in 5 and 10 m regolith thickness, while a layer of regolith 15 m thick was used for larger craters only (diameters between 5 and 26 m). This is due to the pressure wave not being able to reach the underlying layer at ∼10 crater radii away for the craters smaller than 5 m. In the first set of simulations, the underlying substrate was 0% porous bedrock. In the second set of simulations, the underlying layer was represented as 25% porous fractured bedrock. The total combinations of target and impact conditions resulted in 36 different impact simulations (Table 3).

All target representations used the revised Tillotson equation of state for basalt (Wojcicka et al., 2020). Bedrock and fractured bedrock were both described using the ROCK strength model (Collins et al., 2004) Table 4. Density of non-porous basalt was 2,860 kg m^{-3}, and bulk speed of sound ($C_b = \sqrt{\frac{B}{\rho}}$, where B is the bulk modulus) 2,600 m s^{-1}. Fractured bedrock included 25% porosity which was incorporated via $\epsilon - \alpha$ porosity model (e.g., Wünnemann et al., 2006) (Table 5). The density of the fractured bedrock was 2,150 kg m^{-3}, and the bulk speed of sound was 1,558 m s^{-1}. For all scenarios, impactor material remained the same, non-porous basalt with density ρ = 2,860 kg m^{-3} (Rajšić, Miljković, Collins, et al., 2021).

Table 3
Simulations Used Single or Two-Layered Crustal Structure

	Simulation				
Target	1	2	3	4	5
Bedrock (B)	•	•	•	•	•
Fractured bedrock (FB)	•	•	•	•	•
5 m regolith over B	•	•	•	•	•
5 m regolith over FB	•	•	•	•	•
10 m regolith over B	•	•	•	•	•
10 m regolith over FB	•	•	•	•	•
15 m regolith over B			•	•	•
15 m regolith over FB			•	•	•

Note. Impact conditions for each simulation number can be cross-referenced with Table 2. Pressure wave in Simulations 1 and 2 could not reach the bedrock in case of 15 m regolith overlying (fractured) bedrock at ∼10 crater radii away. Therefore, they were not performed in these layered target cases. Bullet point (•) denotes which simulations are matched with what target layer combination.

3.1. Seismic Properties in Layered Targets

The seismic efficiency and seismic moment were calculated for all impact scenarios. The seismic moment was estimated using the approach described by Wojcicka et al. (2020) and Rajšić, Miljković, Wójcicka, et al. (2021) to determine the vertical component of the seismic moment (M_z) (Gudkova et al., 2015; Lognonné et al., 2009): $M_z = \sum_i^n C_p \rho[i] v_z[i] V[i]$, where $\rho[i]$ is the density of material in the cell, $v_z[i]$ is the cell-centered vertical velocity component, $V[i]$ is the cell volume, C_p is the P-wave velocity, and the summation is over all n cells in the target (below the pre-impact level). For vertical impacts, this means that seismic moment is defined as $M_z = C_p p_z$, where p_z is the momentum transferred to the target by the impact (Gudkova et al., 2015; Lognonné et al., 2009; Wojcicka et al., 2020).

Table 4
The Strength Model Parameters Used in Simulations for Bedrock (ROCK, Collins et al., 2004) and Regolith (LUNDD, Lundborg, 1968)

Parameter	Bedrock	Fractured bedrock	Regolith
Strength model	ROCK	ROCK	LUNDD
Bulk porosity	Non-porous	25%	44%
Damaged shear strength (kPa)	10	0	10
Friction damaged	0.6	0.67	0.7
Damaged limiting strength (GPa)	3.5	0.17	0.25
Intact strength (MPa)	10	0.2	–
Intact friction	1.2	1.8	–
Intact limiting strength (GPa)	3.5	0.17	–
Crushing strength (kPa)	–	2×10^3	100

Table 5
The $\epsilon - \alpha$ Porosity Model Parameters Used in Simulations for Different Porosity Targets Wünnemann et al. (2006)

Parameter	Fractured bedrock	Regolith
Initial bulk porosity	25%	44%
Initial distension, α_0	1.33	1.8
Elastic threshold, ϵ_0	-4×10^{-4}	-10^{-4}
Distension at transition, α_x	1.1	1.15
Constant, κ	0.98	0.98
Speed of sound ratio, χ	0.6	0.33

Note. All parameters are unit-less.

To calculate the seismic efficiency k, we applied the same approach as in previous works (e.g., Güldemeister & Wünnemann, 2017; Rajšić, Miljković, Collins, et al., 2021; Wojcicka et al., 2020): $k = \pi x^2 P^2 \Delta t/(\rho C_p E_k)$, where x is the distance from the impact point (in case of layered targets, always measured in the lower layer), P is the pressure amplitude, Δt is the duration of the pressure pulse measured at full-width half maximum, ρ is the bulk density of the target, and E_k is the kinetic energy of the impactor. Data used for calculating seismic efficiency was recorded at pre-selected cells (gauges) positioned equidistant diagonally through the target. Seismic efficiency reported in Table 6 is the average value between the three last gauges (in the case of layered targets positioned in the lower, stronger layer). So, the calculation of density and speed of sound represents the local measurements in the lower layer.

Figure 4 (left) shows how seismic moment varies between different single-layered scenarios (bedrock, fractured bedrock, and regolith) for different impact conditions. Among these single-layered representations, seismic moment varies within an order of magnitude for the same impact momentum. Figure 4 (middle) shows the seismic moment in bedrock, regolith overlying bedrock, and regolith targets. The seismic moment in all layered targets is in agreement up to a factor of 1.3. For small impacts on Mars (smaller than 30 m in crater diameter), the target layering does not have an effect on the seismic moment produced by these impacts. Seismic moment calculated in layered targets shows similar relationship with impact moment shown in Figure 4 (left) for fractured bedrock targets. In Figure 4 (right) we compare the seismic moment and impact momentum relationship in bedrock (the target with the highest calculated seismic moment for all impact scenarios), regolith overlying fractured bedrock, and regolith (target with the lowest calculated seismic moment) are shown. Again, layered targets show a similar relationship with the impact moment calculated for fractured bedrock targets (dotted line Figure 4 (left)). Overall, the relationships shown in Figure 4, indicate that layering plays an effect on seismic moment up to a factor of 4. All the presented relationships between seismic moment and impact momentum were done using the least squares fitting method ($R^2 = 0.99$).

These results provide more information on how seismic moment depends on impact momentum in different target materials (bedrock, fractured bedrock, and layered targets). Scaling relationships shown in Figure 4 are in agreement with Equation 1, showing that the effects of target properties on seismic moment calculated from simulations are negligible. Moreover, these results confirm that seismic moment is very much proportional to the impact momentum, as previously shown on impacts detected in seismic data on the Moon (Gudkova et al., 2011; Lognonné et al., 2009).

Figure 5 shows the relationship between seismic moment and seismic energy. The seismic energy (E_s) is calculated from seismic efficiency $\left(k = \frac{E_s}{E_k}\right)$. For all impact conditions investigated here, seismic efficiency in bedrock targets is of the order of 10^{-3}. These results account for a 1.7 correction factor for the bedrock target to include resolution effects as shown in Rajšić, Miljković, Collins, et al. (2021). In fractured bedrock, the seismic efficiency is of the order of 5×10^{-6}, and in layered targets, this parameter is comparable to the regolith-only targets ($k \sim 10^{-6}$) (Rajšić, Miljković, Collins, et al., 2021; Rajšić, Miljković, Wójcicka, et al., 2021; Wojcicka et al., 2020) as well as lunar observations (Latham et al., 1970; McGarr et al., 1969).

We compared seismic energy calculated in this work to the results of Wojcicka et al. (2020) for regolith like targets, and previous measurements from earthquakes and explosion experiments (Abercrombie, 1995; Mayeda & Walter, 1996; Patton & Walter, 1993; Prieto et al., 2004). In bedrock targets, seismic energy was up to three orders higher than in the case of regolith-like and layered targets for the same impact conditions. In bedrock targets seismic energy, E_s scales with the seismic moment, M, as:

Table 6
Pressure Amplitudes, P, Pressure Pulse Duration, Δt, and Seismic Efficiency, k, Calculated for Different Targets (Cross Reference Numbers With Table 3), and Impact Conditions (Cross Reference Numbers With Table 2)

Simulation	P (Pa)	Δt (s)	k	Target
1	802,897.2	5×10^{-5}	7.9×10^{-4}	Bedrock
2	2,276,971	8.87×10^{-5}	1.16×10^{-3}	
3	3,487,742	1.23×10^{-4}	1.77×10^{-3}	
4	4,503,881	2.36×10^{-4}	1.78×10^{-3}	
5	2,933,324	7.16×10^{-4}	1.16×10^{-3}	
1	19,579.68	3.44×10^{-4}	3.9×10^{-6}	Fractured bedrock
2	34,673.48	7.1×10^{-4}	5.83×10^{-6}	
3	32,500.54	1×10^{-3}	4.09×10^{-6}	
4	38,631.52	2.9×10^{-3}	5.4×10^{-6}	
5	55,088	7.9×10^{-3}	6.36×10^{-6}	
1	4,332.9	1×10^{-3}	5.3×10^{-7}	5 m regolith + bedrock
2	8,451.06	1.9×10^{-3}	2.3×10^{-7}	
3	55,076	3.9×10^{-3}	1.96×10^{-6}	
4	50,991	2.98×10^{-3}	1.17×10^{-6}	
5	90,144.22	2.2×10^{-3}	1.1×10^{-5}	
1	10,481.07	1×10^{-3}	5.95×10^{-7}	5 m regolith + fractured bedrock
2	6,922.09	1×10^{-3}	5.09×10^{-7}	
3	9,601.19	3×10^{-3}	1.17×10^{-6}	
4	25,597.15	3.04×10^{-3}	3.12×10^{-6}	
5	36,809.14	7.4×10^{-3}	3.9×10^{-6}	
1	8,106	7.4×10^{-4}	6.7×10^{-7}	10 m regolith + bedrock
2	7,178.4	2×10^{-3}	2.15×10^{-7}	
3	5,571.03	3.6×10^{-3}	1.5×10^{-7}	
4	7,519.2	8.3×10^{-3}	1.3×10^{-7}	
5	21,822.33	4.6×10^{-3}	8.8×10^{-7}	
1	8,328.35	1.4×10^{-3}	1.59×10^{-6}	10 m regolith + fractured bedrock
2	2,779	2×10^{-3}	1.9×10^{-7}	
3	4,832.82	2.98×10^{-3}	3.07×10^{-7}	
4	6,708.12	5.5×10^{-3}	4.09×10^{-7}	
5	29,936.72	7.12×10^{-3}	3.99×10^{-6}	
3	5,474.72	8.4×10^{-3}	3.6×10^{-7}	15 m regolith bedrock
4	7,402.5	6.6×10^{-3}	1.4×10^{-7}	
5	22,772.8	6.6×10^{-3}	2.08×10^{-7}	
3	3,433.6	2.5×10^{-3}	1.6×10^{-7}	15 m regolith fractured bedrock
4	10,484.93	6.2×10^{-3}	6.2×10^{-7}	
5	24,105.5	3.6×10^{-3}	8.27×10^{-7}	

$$E_s = 2 \times 10^{-4} M \tag{4}$$

In layered targets (Figure 5), the seismic energy, E_s scales with the seismic moment, M, as:

$$E_s = 1 \times 10^{-10} M^{1.4} \tag{5}$$

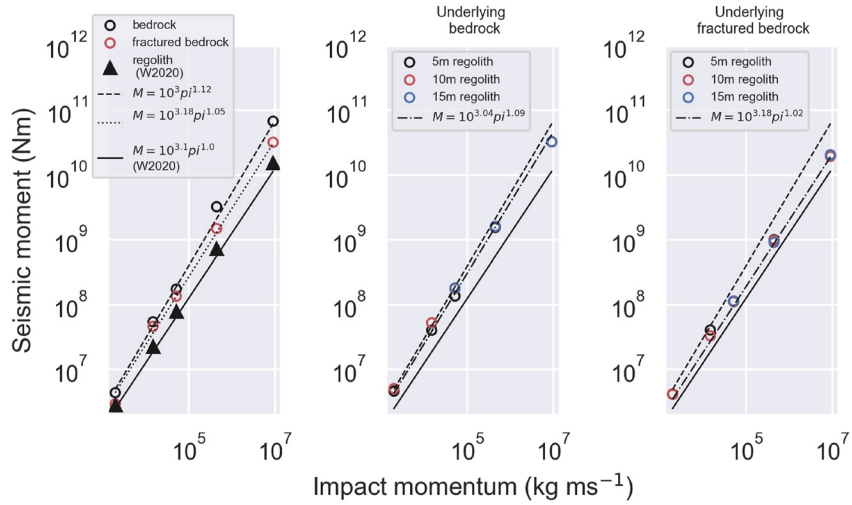

Figure 4. Seismic moment, M, as a function of impact momentum, p_i in: (left) bedrock, fractured bedrock, and regolith targets; (middle) bedrock, regolith overlying bedrock, and regolith targets; (right) bedrock, regolith overlying fractured bedrock, and regolith targets Regolith data is taken from Wojcicka et al. (2020) for comparison with our models (marked as W2020).

which is similar to Equation 3 for the regolith-only targets. This implies that having the weaker layer on top of the bedrock consumes most of the impact energy and results in less seismic energy produced for impacts of the same size. Previous works (Rajšić, Miljković, Collins, et al. (2021)) showed that pressure wave decay with distance from the impact point is much faster in the porous targets.

Using scaling from Figure 5, the seismic energy estimates in different targets as a function of impact momentum are shown in Figure 6. Three orders of magnitude more seismic energy are produced in non-porous targets. However, the scenarios of having impacts on pure bedrock are highly unlikely. Bedrock outcrops alone are rare, and the chances of impacting straight on these outcrops are even smaller. Moreover, the pressure wave generated by the impact also needs to go through different media to be detected on the seismometer. We know that InSight

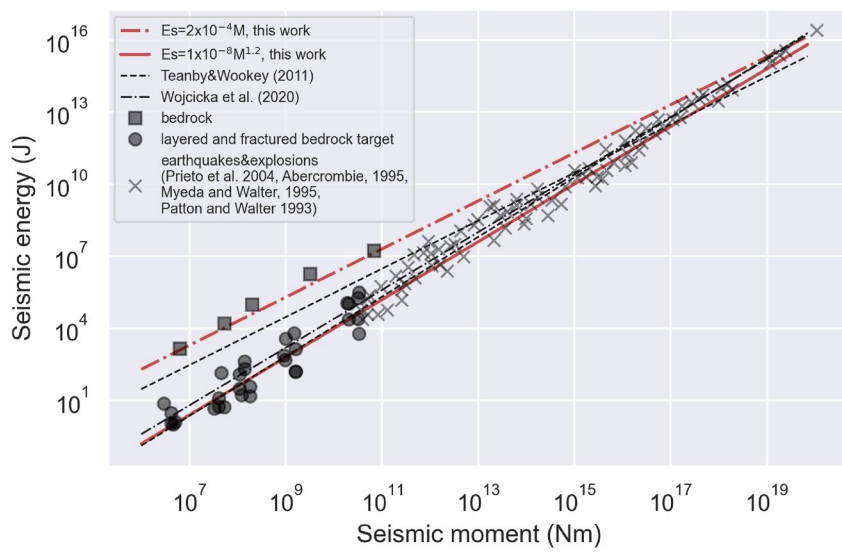

Figure 5. Seismic energy as a function of the seismic moment, in bedrock (squares), fractured bedrock, and layered targets (filled circles). Red lines are from this work, and black lines are from Wojcicka et al. (2020) (*W2020*) and Teanby and Wookey (2011) (*TW2011*). Previous works (Abercrombie, 1995; Mayeda & Walter, 1996; Patton & Walter, 1993; Prieto et al., 2004) on earthquakes and explosions show a good fit with layered/regolith target analogs (marked with x).

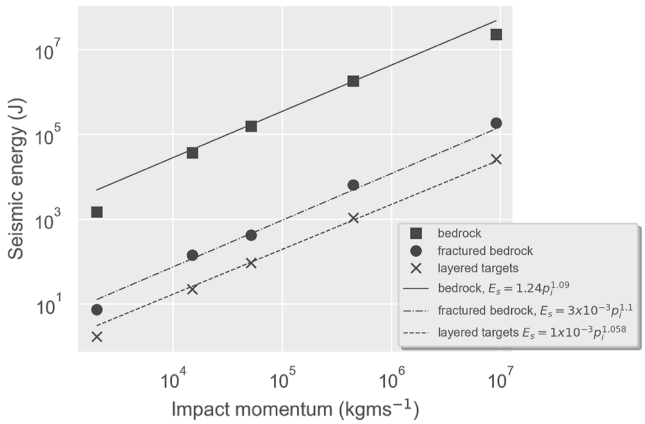

Figure 6. Seismic energy as a function of the impact momentum, in bedrock (black line), fractured bedrock (dash-dotted black line), and layered targets (dashed black line). Two orders of magnitude more seismic energy are produced in stronger targets for the same impact momentum. Markers are denoted for the impact momentum of the scenarios investigated in this work.

is located in a regolith-covered region. Therefore, the seismic moment generated from impacts on Mars would most likely be in the ranges proposed for layered and regolith-like targets.

4. Comparison Between Modeling Results and the New Impacts Confirmed in Seismic Data

During the operation of NASA's InSight Mission on Mars, several small impacts were identified in both seismic data collected by the seismometer instrument (the Seismic Experiment for Interior Structure [SEIS]) and images taken by orbiting spacecraft (Garcia et al., 2022). The diameters of craters first detected using seismic data (seismic events S0793a, S0986c, and S0981c; InSight Marsquake Service (2022b)) were measured from orbital images to be 3.9, 6.1, and 7.24 m, respectively. The distances between SEIS and these craters were measured to be 85.1, 91.1, and 244 km. Two much larger fresh impact craters (130–150 m diameter, at distances of 3,460 and 7,455 km from InSight lander) were also recently detected on Mars (Posiolova et al., 2022). Both impacts produced large magnitude seismic events (moment magnitude > 4), making them two of the largest seismic events detected on Mars (Horleston et al., 2022; InSight Marsquake Service, 2022a) by InSight. These new impact detections provide the opportunity for comparison with the results of our numerical impact models.

The small impacts reported in Garcia et al. (2022) have moment magnitudes of 1.4, 1.6, and 1.2, assigned by MQS (InSight Marsquake Service, 2022b). The seismic moment calculated from these moment magnitudes results in an overestimation (order of 10^{15} Nm, Böse et al., 2021) because these moment estimates are computed with an a priori source depth of 50 km instead of the surface location of impact, and are valid only for source distances further than 150 km. In addition, MQS calculations of the seismic event magnitude were made from epicentral distances that are different to distances confirmed in orbital imaging (see Garcia et al. (2022)). Therefore, in Garcia et al. (2022) SPECFEM2D-DG-LNS (Martire et al., 2022) models were used to estimate seismic moment. Here, we report updated values of seismic moment estimates with a complete 2D-3D correction instead of the approximation used in Garcia et al. (2022). These improved seismic moment values are a factor of 10–20, smaller than previously estimated. This correction is significant but similar to the one-order-of-magnitude error induced by our poor knowledge of the seismic quality factors in the crust.

The new seismic moment values are shown in Table 7. Seismic moment estimates from models using different seismic quality factors Q show ~6 times difference in the case of impact events detected at ~80–90 km from SEIS (S0986c and S0793a). Because impact event S0981c was detected at much larger distance (244 km) than the other two events, the sensitivity of the seismic moment to the Q used in SPECEFEM2D-DG-LNS is much higher (~2 orders of magnitude difference between low and high Q moments). This is also observed in Figure 7, where SPECEFEM2D-DG-LNS models with $Q = 2{,}000$ are consistent with results from our iSALE models, and the S0981c shows two orders of magnitude difference when lower seismic quality is considered.

The closer, large impact reported in Posiolova et al. (2022) (S1094b), detected at a distance of 3,460 km from InSight lander, was used for further seismic source analysis. For this magnitude 4 event, MQS estimated a seismic moment of ~10^{15} Nm, using seismic velocities at 50 ± 30 km depth (Böse et al., 2021). Because seismic attenuation at this large distance plays a significant role, SPECFEM2D-DG-LNS models were not made for this event. However, additional seismic source modeling suggested the appropriate seismic source depth of the impact-generated wave was ~50 m Posiolova et al. (2022). Correcting the seismic moment for the large difference in seismic velocity and density between 50 m and 50 km resulted in a moment of

Table 7
Seismic Moment as Measured From SPECFEM2D-DG-LNS (Martire et al., 2022) Models for Different Seismic Quality Factor (Q = 100 and Q = 2,000)

Impact event	Median vertical impact momentum (kg ms^{-1})	Estimated distance (in km)	Seismic moment (Nm) $Q = 100$	Seismic moment (Nm) $Q = 2{,}000$
S0793a	27,000	85.1	1.85×10^8	3.08×10^7
S0986c	89,500	91.1	4.56×10^8	7.36×10^7
S0981c	202,000	244	8.66×10^{10}	5.49×10^8

Note. The new models include 2D-3D correction, which resulted in 10–20 times smaller measurements than reported in Garcia et al. (2022). The results are compared to iSALE-2D models in Figure 7. Impact momentum and estimated distance from the seismometer are as reported in Garcia et al. (2022).

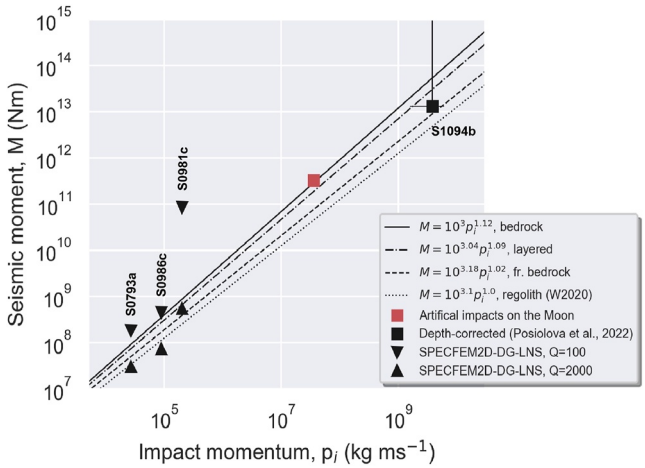

Figure 7. Seismic moment, M, as a function of impact momentum, p_i, compared to the results of the SPECFEM2D-DG-LNS (Martire et al., 2022) models that included different seismic quality factor (reverse triangles—$Q = 100$, triangles—$Q = 2{,}000$). Our results show an agreement with depth-corrected MQS measurements for large impact reported in Posiolova et al. (2022) and with artificial impacts on the Moon (Lognonné et al., 2009; Plescia et al., 2016).

$\sim 10^{13}$ Nm, approximately two orders of magnitude lower than the MQS seismic moment ($\sim 10^{15}$ Nm). The depth corrected seismic moment reported by (Posiolova et al., 2022) is in good agreement with results from our numerical models (Figure 7).

Overall, our results show agreement with seismic moment measured for artificial impacts on the Moon (Lognonné et al., 2009; Plescia et al., 2016) and depth-corrected moment values for the seismic source of the large impact event (Posiolova et al., 2022). For closer, small-impact events results of our models agree with seismic moments derived from SPECFEM2D-DG-LNS models when $Q = 2{,}000$ is applied. However, the SPECFEM2D-DG-LNS models show that further direct comparison between seismic moment measurements requires a better understanding of seismic attenuation in the Martian crust.

5. Conclusion

The work presented here included estimates of regolith thickness using REC (RECs). We mapped 1,155 simple, fresh craters with diameters between 2.2 and 103 m. They were classified according to the presence of the boulders in the ejecta into REC and nREC. The RECs provided a thickness of the regolith layer. The nRECs provided a lower limit for the regolith thickness, given they had not excavated any stronger layer underneath. We find that 1.4% of total counted craters are REC (16 craters among 1,155 mapped in total). All RECs are fresh and were identified to belong to the first two degradation classes, according to Warner et al. (2017). Using the factor of 0.084 and measured crater diameters, we estimated regolith thickness to be between 4 and 9 m. Mapping of craters and regolith thickness estimate was done in the vicinity of one of the recently formed impact craters on Mars. The geological unit of interest was the Late Amazonian unit. This unit is younger than early Hesperian unit where the InSight lander is situated. Consequently, regolith thickness observed in this small area was two times thinner (4–9 m) than previously estimated for the InSight landing site (3–17 m, Warner et al., 2017).

The second part of the paper was focused on numerical simulations using iSALE-2D shock physics code. We adopted regolith thickness estimates and developed layered target models. Impact momentum was varied between 7×10^2 and 9.08×10^6 kg m s^{-1} to simulate pressure wave propagation for impacts that would form craters between 1.5 and 26 m in diameter. These scenarios were tested in single-layered targets bedrock (0% porosity) and fractured bedrock (25% porosity), as well as in layered targets. Layered targets were modeled as two layers, where regolith (44% porous basalt) varies in thickness between 5, 10, and 15 m. The underlying layer was also varied; it was either bedrock or fractured bedrock. These results were also compared to the data made for regolith-like targets in previous works (Rajšić, Miljković, Collins, et al., 2021; Wojcicka et al., 2020).

We found that the presence of the upper, low-cohesion layer consumes more impact energy and momentum, which results in less seismic energy produced in layered targets than in single-layer bedrock-like targets. Both the duration of the pressure pulse and the pressure wave amplitude are affected by a shock wave moving radially through the regolith layer. So, the resulting seismic efficiency for small craters on Mars in regolith-like and layered targets is of the order of $\sim 10^{-6}$. In fractured bedrock target it is half an order of magnitude higher while for non-fractured, bedrock targets it is three orders of magnitude higher ($\sim 10^{-3}$). Unlike seismic energy, the seismic moment shows less dependence on target properties and more on the impact momentum. Even between single-layer bedrock targets and regolith-like targets, the resulting seismic moment is in agreement up to a factor of 4. Simulation outcomes suggested a relationship between seismic moment and impact momentum and seismic moment and seismic energy. These newly constrained relationships were applied to the first newly formed craters on Mars observed in seismic data. This extensive numerical modeling work, developed for a range of upper Martian crust analogs, could be used to estimate impact detectability in seismic data.

Data Availability Statement

Data used in this paper, including the list of locations of all mapped craters and input files for iSALE-2D models, are available in the open access repository: Rajšić (2022). Data used to compare numerical models to InSight observations is available at: InSight Marsquake Service (2022a, 2022b). HiRISE tile can be accessed at: https://www.uahirise.org/ESP_047376_1865.

Acknowledgments
We gratefully acknowledge the developers of iSALE (https://github.com/isale-code/isale-wiki/wiki). AR and KM are fully funded by the Australian Research Council (DE180100584, DP180100661, and FT210100063). CB is funded under the Curtin Research Fellowship. NW and GSC are funded by the UK Space Agency (Grants ST/S001514/1 and ST/T002026/1). RFG and PL acknowledge the French Space Agency CNES and ANR (ANR-14-CE36-0012-02 and ANR-19-CE31-0008-08) for funding the InSight Science analysis. RFG thank CALMIP (Toulouse, France, project p1404) computing center for HPC resources. AL is funded by the Australian Research Council (DP210100336). This is InSight Contribution Number 254. Open access publishing facilitated by Curtin University, as part of the Wiley - Curtin University agreement via the Council of Australian University Librarians.

References

Abercrombie, R. E. (1995). Earthquake source scaling relationships from- 1 to 5 ml using seismograms recorded at 2.5-km depth. *Journal of Geophysical Research*, *100*(B12), 24015–24036. https://doi.org/10.1029/95jb02397

Amsden, A., Ruppel, H., & Hirt, C. (1980). *Sale: A simplified ale computer program for fluid flow at all speeds* (Tech. Rep.). Los Alamos Scientific Laboratory.

Banerdt, W. B., Smrekar, S. E., Banfield, D., Giardini, D., Golombek, M., Johnson, C. L., et al. (2020). Initial results from the InSight mission on Mars. *Nature Geoscience*, *13*(3), 1–7. https://doi.org/10.1038/s41561-020-0544-y

Bart, G. D., Nickerson, R. D., Lawder, M. T., & Melosh, H. (2011). Global survey of lunar regolith depths from LROC images. *Icarus*, *215*(2), 485–490. https://doi.org/10.1016/j.icarus.2011.07.017

Benedix, G., Lagain, A., Chai, K., Meka, S., Anderson, S., Norman, C., et al. (2020). Deriving surface ages on Mars using automated crater counting. *Earth and Space Science*, *7*(3), e2019EA001005. https://doi.org/10.1029/2019ea001005

Böse, M., Stähler, S. C., Deichmann, N., Giardini, D., Clinton, J., Lognonné, P., et al. (2021). Magnitude scales for marsquakes calibrated from insight data. *Bulletin of the Seismological Society of America*, *111*(6), 3003–3015. https://doi.org/10.1785/0120210045

Clinton, J., & Euchner, F. (2021). Mars seismic catalogue, insight mission; v5 2021-01-04.

Collins, G. S., Melosh, H. J., & Ivanov, B. A. (2004). Modeling damage and deformation in impact simulations. *Meteoritics & Planetary Sciences*, *39*(2), 217–231. https://doi.org/10.1111/j.1945-5100.2004.tb00337.x

Cooper, M. R., Kovach, R. L., & Watkins, J. S. (1974). Lunar near-surface structure. *Reviews of Geophysics*, *12*(3), 291–308. https://doi.org/10.1029/rg012i003p00291

Daubar, I., Dundas, C., McEwen, A., Gao, A., Wexler, D., Piqueux, S., et al. (2022). New craters on Mars: An updated catalog. *Journal of Geophysical Research: Planets*, *127*(7), e2021JE007145. https://doi.org/10.1029/2021je007145

Daubar, I., Lognonné, P., Teanby, N., Collins, G., Clinton, J., Stähler, S., et al. (2020). A new crater near insight: Implications for seismic impact detectability on Mars. *Journal of Geophysical Research: Planets*, *125*(8), e2020JE006382. https://doi.org/10.1029/2020je006382

Daubar, I., Lognonné, P., Teanby, N. A., Miljkovic, K., Stevanović, J., Vaubaillon, J., et al. (2018). Impact-seismic investigations of the insight mission. *Space Science Reviews*, *214*(8), 1–68. https://doi.org/10.1007/s11214-018-0562-x

Daubar, I., McEwen, A. S., Byrne, S., Kennedy, M., & Ivanov, B. (2013). The current Martian cratering rate. *Icarus*, *225*(1), 506–516. https://doi.org/10.1016/j.icarus.2013.04.009

Daubar, I. J., Atwood-Stone, C., Byrne, S., McEwen, A. S., & Russell, P. (2014). The morphology of small fresh craters on Mars and the moon. *Journal of Geophysical Research: Planets*, *119*(12), 2620–2639. https://doi.org/10.1002/2014je004671

Duennebier, F., & Sutton, G. H. (1974). Meteoroid impacts recorded by the short-period component of Apollo 14 lunar passive seismic station. *Journal of Geophysical Research*, *79*(29), 4365–4374. https://doi.org/10.1029/jb079i029p04365

Garcia, R. F., Daubar, I. J., Beucler, É., Posiolova, L. V., Collins, G. S., Lognonné, P., et al. (2022). Newly formed craters on Mars located using seismic and acoustic wave data from insight. *Nature Geoscience*, *15*(10), 774–780. https://doi.org/10.1038/s41561-022-01014-0

Golombek, M., Warner, N., Grant, J., Hauber, E., Ansan, V., Weitz, C., et al. (2020). Geology of the InSight landing site on Mars. *Nature Communications*, *11*(1), 1–11. https://doi.org/10.1038/s41467-020-14679-1

Grieve, R., Robertson, P., & Dence, M. (1981). Constraints on the formation of ring impact structures, based on terrestrial data. In *Multi-ring basins: Formation and evolution* (pp. 37–57).

Gudkova, T., Lognonné, P., & Gagnepain-Beyneix, J. (2011). Large impacts detected by the Apollo seismometers: Impactor mass and source cutoff frequency estimations. *Icarus*, *211*(2), 1049–1065. https://doi.org/10.1016/j.icarus.2010.10.028

Gudkova, T., Lognonné, P., Miljković, K., & Gagnepain-Beyneix, J. (2015). Impact cutoff frequency–momentum scaling law inverted from Apollo seismic data. *Earth and Planetary Science Letters*, *427*, 57–65. https://doi.org/10.1016/j.epsl.2015.06.037

Güldemeister, N., & Wünnemann, K. (2017). Quantitative analysis of impact-induced seismic signals by numerical modeling. *Icarus*, *296*, 15–27. https://doi.org/10.1016/j.icarus.2017.05.010

Hermalyn, B., & Schultz, P. H. (2011). Time-resolved studies of hypervelocity vertical impacts into porous particulate targets: Effects of projectile density on early-time coupling and crater growth. *Icarus*, *216*(1), 269–279. https://doi.org/10.1016/j.icarus.2011.09.008

Hoerth, T., Schäfer, F., Nau, S., Kuder, J., Poelchau, M. H., Thoma, K., & Kenkmann, T. (2014). In situ measurements of impact-induced pressure waves in sandstone targets. *Journal of Geophysical Research: Planets*, *119*(10), 2177–2187. https://doi.org/10.1002/2014je004616

Holsapple, K. A. (1993). The scaling of impact processes in planetary sciences. *Annual Review of Earth and Planetary Sciences*, *21*(1), 333–373. https://doi.org/10.1146/annurev.ea.21.050193.002001

Horleston, A. C., Clinton, J. F., Ceylan, S., Giardini, D., Charalambous, C., Irving, J. C., et al. (2022). The far side of Mars: Two distant marsquakes detected by insight. *The Seismic Record*, *2*(2), 88–99. https://doi.org/10.1785/0320220007

InSight Marsquake Service. (2022a). *Mars seismic catalogue, insight mission; v11 2022-07-01*. ETHZ, IPGP, JPL, ICL, Univ. Bristol. Retrieved from https://www.insight.ethz.ch/seismicity/catalog/v11

InSight Marsquake Service. (2022b). *Mars seismic catalogue, insight mission; v9 2022-01-01*. ETHZ, IPGP, JPL, ICL, Univ. Bristol. Retrieved from https://www.insight.ethz.ch/seismicity/catalog/v9

Kneissl, T., van Gasselt, S., & Neukum, G. (2011). Map-projection-independent crater size-frequency determination in GIS environments—New software tool for ArcGIS. *Planetary and Space Science*, *59*(11–12), 1243–1254. https://doi.org/10.1016/j.pss.2010.03.015

Lagain, A., Benedix, G., Servis, K., Baratoux, D., Doucet, L., Rajšic, A., et al. (2021). The Tharsis mantle source of depleted shergottites revealed by 90 million impact craters. *Nature Communications*, *12*(1), 1–9. https://doi.org/10.1038/s41467-021-26648-3

Latham, G., Ewing, M., Dorman, J., Press, F., Toksoz, N., Sutton, G., et al. (1970). Seismic data from man-made impacts on the moon. *Science*, *170*(3958), 620–626. https://doi.org/10.1126/science.170.3958.620

Lognonné, P., Le Feuvre, M., Johnson, C. L., & Weber, R. C. (2009). Moon meteoritic seismic hum: Steady state prediction. *Journal of Geophysical Research*, *114*(E12), E12003. https://doi.org/10.1029/2008je003294

Lundborg, N. (1968). Strength of rock-like materials. *International Journal of Rock Mechanics and Mining Sciences & Geomechanics Abstracts*, *5*, 427–454. https://doi.org/10.1016/0148-9062(68)90046-6

Martire, L., Martin, R., Brissaud, Q., & Garcia, R. (2022). SPECFEM2D-DG, an open-source software modelling mechanical waves in coupled solid–fluid systems: The linearized Navier–Stokes approach. *Geophysical Journal International*, *228*(1), 664–697. https://doi.org/10.1093/gji/ggab308

Matsue, K., Yasui, M., Arakawa, M., & Hasegawa, S. (2020). Measurements of seismic waves induced by high-velocity impacts: Implications for seismic shaking surrounding impact craters on asteroids. *Icarus*, *338*, 113520. https://doi.org/10.1016/j.icarus.2019.113520

Mayeda, K., & Walter, W. R. (1996). Moment, energy, stress drop, and source spectra of western United States earthquakes from regional coda envelopes. *Journal of Geophysical Research*, *101*(B5), 11195–11208. https://doi.org/10.1029/96jb00112

McEwen, A. S., Eliason, E. M., Bergstrom, J. W., Bridges, N. T., Hansen, C. J., Delamere, W. A., et al. (2007). Mars reconnaissance orbiter's high resolution imaging science experiment (HIRISE). *Journal of Geophysical Research*, *112*(E5), E05S02. https://doi.org/10.1029/2005je002605

McGarr, A., Latham, G. V., & Gault, D. E. (1969). Meteoroid impacts as sources of seismicity on the moon. *Journal of Geophysical Research*, *74*(25), 5981–5994. https://doi.org/10.1029/jb074i025p05981

McMullan, S., & Collins, G. (2019). Uncertainty quantification in continuous fragmentation airburst models. *Icarus*, *327*, 19–35. https://doi.org/10.1016/j.icarus.2019.02.013

Melosh, H. J. (1989). *Impact cratering: A geologic process*. ICGP.

Patton, H. J., & Walter, W. R. (1993). Regional moment: Magnitude relations for earthquakes and explosions. *Geophysical Research Letters*, *20*(4), 277–280. https://doi.org/10.1029/93gl00298

Plescia, J., Robinson, M., Wagner, R., & Baldridge, R. (2016). Ranger and Apollo S-IVB spacecraft impact craters. *Planetary and Space Science*, *124*, 15–35. https://doi.org/10.1016/j.pss.2016.01.002

Pomeroy, P. W. (1963). Long period seismic waves from large, near-surface nuclear explosions. *Bulletin of the Seismological Society of America*, *53*(1), 109–149. https://doi.org/10.1785/bssa0530010109

Posiolova, L., Lognonné, P., Banerdt, W., Clinton, J., Collins, G., Kawamura, T., et al. (2022). Largest recent impact craters on Mars: Orbital imaging and surface seismic co-investigation. *Science*, *378*(6618), 412–417. https://doi.org/10.1126/science.abq7704

Prieto, G. A., Shearer, P. M., Vernon, F. L., & Kilb, D. (2004). Earthquake source scaling and self-similarity estimation from stacking P and S spectra. *Journal of Geophysical Research*, *109*(B8), B08310. https://doi.org/10.1029/2004jb003084

Quaide, W. L., & Oberbeck, V. R. (1968). Thickness determinations of the lunar surface layer from lunar impact craters. *Journal of Geophysical Research*, *73*(16), 5247–5270. https://doi.org/10.1029/jb073i016p05247

Rajšić, A. (2022). Seismic efficiency and seismic moment for small craters on Mars formed in layered uppermost crust. https://doi.org/10.5281/zenodo.7378086

Rajšić, A., Miljković, K., Collins, G., Wünnemann, K., Daubar, I., Wójcicka, N., & Wieczorek, M. (2021). Seismic efficiency for simple crater formation in the Martian top crust analogue. *Journal of Geophysical Research: Planets*, *126*(2), 2020JE006662. https://doi.org/10.1029/2020JE006662

Rajšić, A., Miljković, K., Wójcicka, N., Collins, G., Onodera, K., Kawamura, T., et al. (2021). Numerical simulations of the Apollo S-IVB artificial impacts on the moon. *Earth and Space Science*, *8*(12), e2021EA001887. https://doi.org/10.1029/2021ea001887

Rennilson, J., Dragg, J., Morris, E., Shoemaker, E., & Turkevich, A. (1966). Surveyor i mission report. *NASA Technical Report*, *III*(32–1023), 188–212.

Richardson, J., & Kedar, S. (2013). An experimental investigation of the seismic signal produced by hypervelocity impacts. In *Lunar and planetary science conference* (p. 2863).

Schultz, P., & Gault, D. (1975). Seismically induced modification of lunar surface features. In *Lunar and planetary science conference proceedings*, (Vol. 6, pp. 2845–2862).

Schultz, P. H., & Anderson, R. R. (1996). Asymmetry of the Manson impact structure: Evidence for impact angle and direction. *Geological Society of America Special Papers*, *302*, 397–417. https://doi.org/10.1130/0-8137-2302-7.397

Shishkin, N. (2007). Seismic efficiency of a contact explosion and a high-velocity impact. *Journal of Applied Mechanics and Technical Physics*, *48*(2), 145–152. https://doi.org/10.1007/s10808-007-0019-6

Shoemaker, E., Batson, R., Holt, H., Morris, E., Rennilson, J., & Whitaker, E. (1969). Observations of the lunar regolith and the Earth from the television camera on surveyor 7. *Journal of Geophysical Research*, *74*(25), 6081–6119. https://doi.org/10.1029/jb074i025p06081

Shoemaker, E., & Morris, E. (1970). Geology: Physics of fragmental debris. *Icarus*, *12*(2), 188–212. https://doi.org/10.1016/0019-1035(70)90072-2

Smith, D. E., Zuber, M. T., Frey, H. V., Garvin, J. B., Head, J. W., Muhleman, D. O., et al. (2001). Mars orbiter laser altimeter: Experiment summary after the first year of global mapping of Mars. *Journal of Geophysical Research*, *106*(E10), 23689–23722. https://doi.org/10.1029/2000je001364

Tanaka, K., Skinner, J., Fortezzo, C., Hare, T., Irwin, R., Platz, T., et al. (2014). TheNew'Geology of Mars: Top ten results of post-viking global mapping and crater-dating. In *Eighth international conference on mars*, (Vol. 1791, p. 1087).

Tanaka, K., Skinner, J., Jr., Dohm, J., Irwin, R., III, Kolb, E., Fortezzo, C., et al. (2014). Geologic map of mars: Us geological survey scientific investigations map 3292. scale 1: 20,000,000 (p. 43).

Teanby, N. (2015). Predicted detection rates of regional-scale meteorite impacts on Mars with the insight short-period seismometer. *Icarus*, *256*, 49–62. https://doi.org/10.1016/j.icarus.2015.04.012

Teanby, N., & Wookey, J. (2011). Seismic detection of meteorite impacts on Mars. *Physics of the Earth and Planetary Interiors*, *186*(1–2), 70–80. https://doi.org/10.1016/j.pepi.2011.03.004

Walker, J. D. (2003). Loading sources for seismological investigation of asteroids and comets. *International Journal of Impact Engineering*, *29*(1–10), 757–769. https://doi.org/10.1016/j.ijimpeng.2003.10.022

Warner, N., Golombek, M., Sweeney, J., Fergason, R., Kirk, R., & Schwartz, C. (2017). Near surface stratigraphy and regolith production in southwestern Elysium Planitia, Mars: Implications for Hesperian-Amazonian terrains and the insight lander mission. *Space Science Reviews*, *211*(1), 147–190. https://doi.org/10.1007/s11214-017-0352-x

Watkins, J. S., & Kovach, R. L. (1973). Seismic investigation of the lunar regolith. In *Lunar and planetary science conference proceedings*, (Vol. 4, p. 2561).

Wilcox, B., Robinson, M., Thomas, P., & Hawke, B. (2005). Constraints on the depth and variability of the lunar regolith. *Meteoritics & Planetary Sciences*, *40*(5), 695–710. https://doi.org/10.1111/j.1945-5100.2005.tb00974.x

Wojcicka, N., Collins, G. S., Bastow, I. D., Teanby, N. A., Miljković, K., Rajšić, A., et al. (2020). The seismic moment and seismic efficiency of small impacts on Mars. *Journal of Geophysical Research: Planets*, *125*(10), e2020JE006540. https://doi.org/10.1029/2020je006540

Wünnemann, K., Collins, G., & Melosh, H. (2006). A strain-based porosity model for use in hydrocode simulations of impacts and implications for transient crater growth in porous targets. *Icarus*, *180*(2), 514–527. https://doi.org/10.1016/j.icarus.2005.10.013

Yasui, M., Matsumoto, E., & Arakawa, M. (2015). Experimental study on impact-induced seismic wave propagation through granular materials. *Icarus*, *260*, 320–331. https://doi.org/10.1016/j.icarus.2015.07.032